3D-architected alkaline-earth perovskites

J.P. Winczewski[1,,#], J. Arriaga Dávila [1,#], M. Herrera-Zaldívar[2], F. Ruiz-Zepeda,[3,4], R. Margoth Córdova-Castro[5], Camilo R. Pérez de la Vega[6], C. Cabriel[6], I. Izeddin[6], J.G.E. Gardeniers[1], and A. Susarrey-Arce[1,*]*

[1]Mesoscale Chemical Systems, MESA+ Institute, University of Twente, P.O. Box 217, Enschede, 7500 AE, The Netherlands

[2]Centro de Nanociencias y Nanotecnología, Universidad Nacional Autónoma de México, Km 107 Carretera Tijuana-Ensenada, Ensenada, Baja California, C.P. 22800, México

[3]National Institute of Chemistry, Hajdrihova 19, Ljubljana, SI-1000 Slovenia

[4]Department of Physics and Chemistry of Materials, Institute of Metals and Technology, Lepi pot 11, Ljubljana, Slovenia

[5]Department of Physics, University of Ottawa, Ottawa, Ontario K1N 6N5, Canada

[6]Institut Langevin, ESPCI Paris, CNRS, PSL University, 1 rue Jussieu, Paris, 75005 France

*Corresponding author(s): j.p.winczewski@utwente.nl; j.g.e.gardeniers@utwente.nl; a.susarreyarce@utwente.nl

#These authors contributed equally to this work

Abstract

Three-dimensional (3D) ceramic architectures are captivating geometrical features with an immense demand in photonics. Here, we develop an additive manufacturing (AM) approach for printing alkaline-earth perovskite 3D microarchitectures. The newly developed approach enables custom-made photoresists suited for two-photon lithography, permitting the production of alkaline-earth perovskite ($BaZrO_3$, $CaZrO_3$, and $SrZrO_3$) 3D structures shaped in the form of octet-truss lattices, gyroids or inspired architectures like sodalite zeolite, and C_{60} buckyball with micrometric and nanometric feature sizes. Alkaline-earth perovskite morphological, structural, and chemical characteristics are studied. The optical properties of such perovskite architectures are investigated using cathodoluminescence and wide-field photoluminescence emission to estimate the lifetime rate and defects in $BaZrO_3$, $CaZrO_3$, and $SrZrO_3$. From a broad perspective, our AM methodology facilitates the production of 3D-structured mixed oxides. Our findings are the first steps toward dimensionally-refined high refractive index ceramics for micro-optics and other terrains like (photo)catalysis.

WILEY-VCH

1. Introduction

Perovskite is the trivial name of a category of significant compounds with crystal structures analogous to $CaTiO_3$. Perovskites are typically composed of alkali, alkali earth, or rare-earth (A), transition metal cations (B), and anions (X), usually oxide or halides.[1] Various forms and cation-pairings have been engineered or found in nature, in which the A-site cations generally have larger radii than B.[1] The simplest oxide perovskite is an ABX_3 with a cubic structure composed of BX_6 octahedra sharing corners with 12-fold coordinated A sites located in the center of the cube of eight BX_6 units.[2] Beyond perfect perovskite crystals, distorted perovskites of reduced symmetries, such as triclinic, monoclinic, tetragonal, rhombohedral, and orthorhombic,[3] can be derived by combining A and B cations of particular ionic radii and electronegativity.[1] Within this construction, electronic structure and dipole moment can be altered by BX_6 octahedra tilting, which modifies the crystal field effect of the perovskite lattice, enabling their applicability in materials sciences.[4,5]

Among perovskites, alkaline-earth zirconates are attractive materials with functionality tunable by their chemical composition, e.g., A = Sr, Ba, Ca, and B = Zr.[6,7] The added value of alkaline-earth zirconates can be found in emerging fields where materials scientists can contribute, like 3D micro-optics, light-emitting devices, and photonic crystals, where high-refractive index materials are much desired.[8] Among the alkaline-earth zirconates, $SrZrO_3$ has high dielectric permittivity and low microwave loss relevant for communication in small dielectric resonator antennas.[9] Other applications of $SrZrO_3$ include, e.g., next-generation nonvolatile memory.[10] For other alkaline-earth zirconates, like $BaZrO_3$ and $CaZrO_3$, applications in wireless communication[11] and inorganic luminescent materials[12] can be found. From these examples, the alkaline-earth zirconates application

WILEY-VCH

range has gradually expanded and is expected to grow due to the demand for 3D ceramic microsystems.[8]

A commonwealth in $SrZrO_3$, $BaZrO_3$, and $CaZrO_3$ is the need for spatial organization, where cellular components of the specific composition are assembled and tailored to control chemical reaction performance or light-matter interaction. From this perspective, chemical technology is an important field where 3D architectures, like alkaline-earth zirconates, can also contribute. Alkaline-earth zirconates can then be geometrically designed catalysts to bridge between nanometer and micrometer length scales and act as a staircase to reach an understanding between chemical processes at the molecular level and the bulk continuum, where mass transport and diffusion might be rate-determining steps. Light-induced processes, such as photocatalysis, should not be excluded. In this case, 3D photocatalysts will require light management to modulate light-matter interaction (light absorption, reflection, and scattering) within a hierarchical architecture to promote carrier generation and induce chemical transformation, such as H_2 evolution from water splitting.[13]

Limited examples of alkaline perovskites exist in literature. These are scaffolds for bone regeneration,[14] piezoelectric,[15] and high-refractive index photonic crystals.[16,17] The lack of precursor versatility options is perhaps a potential reason for such limited examples. Like printed metal oxides, perovskites might suffer from particle-laden photoresists utilized in UV lithography, which is not applicable in such a realm. Under intense illumination, the dispersed particulate media strongly scatter light required for the photopolymerization, which exposes volumes higher than the desired voxel size. In turn, the resolution and attainable feature sizes are strongly compromised. Marino and co-authors have presented the additive manufacturing of composite piezoelectric microarchitectures printed using an Ormocomp-based photoresin with dispersed $BaZrO_3$

nanoparticles (10 wt.%).[18] However, the authors have not studied the possibility of achieving solid ceramic 3D microarchitectures. Solid SiO_2 and ZrO_2 miniaturized replicas of the 3D microarchitectures have been achieved by using higher concentrations of nanoparticles (40 − 45 wt.%) and thermal processing.[19,20] To circumvent the aggregation and provide dispersion stability, nanoparticles (~ 5 - 10 nm) can be either surface-functionalized or used along the binder matrix (~ 40 nm SiO_2 with hydroxyethyl methacrylate and trimethylolpropane ethoxylate triacrylate).[19–21]

Currently, the established method providing genuine 3D shaping of solid-beam metal oxide microarchitectures relies on tailored solutions for two-photon lithography (TPL).[22] Custom organic-inorganic photoresists are typically used to print metal-rich microarchitectures, subsequently annealed at elevated temperatures in the air to form self-miniaturized metal-oxide replicas. Examples of materials accomplished with the custom TPL-dedicated photoresists composed of organic-inorganic polymers include TiO_2,[23] ZrO_2,[20,24] ZnO,[25] or SnO_2.[26] Recently, Bauer *et al*. presented the AM of nanoscale optical-grade glass architectures *via* a sinterless approach, utilizing a photoresin based on polyhedral oligomeric silsesquioxanes.[27] Reports on microarchitectures of more complex chemical composition often rely on the application of sol-gel photoresins based on a Si backbone, which permits the fabrication of, e.g., mixed SiO_2 and ZrO_2,[28] or SiO_2 and TiO_2,[29] $SiOC$,[30,31] $SiCN$,[32] or $SiBCN$.[33] Alternatively, salts can be introduced to the photoresin to yield, i.e., $Y_3Al_5O_{12}$,[34] or dope ZrO_2 with lanthanides.[24,35] The true uniqueness of such an approach is the possibility of tuning the chemical composition of resulting ceramics. From the previous examples, it is fair to say that there is an uttermost interest in elaborating solutions enabling the accurate structuring of complex oxide systems, like perovskites in 3D, to stimulate the thriving interfacing of material sciences in AM and overarch other science domains, like ceramic micro-optics.[8]

WILEY-VCH

Although 3D-architected perovskites are attractive in various fields, an additional key limitation is derived from carbon-rich mixtures of organic-inorganic polymers used during printing. The TPL-dedicated photoresists demand precise precursor stoichiometry to reduce side product formation (i.e., non-stoichiometric mixtures, separated simple oxides) and reach the targeted alkaline-earth perovskite crystallographic phases.[36,37] In the zirconate synthesis, alkaline-earth oxide (AO) and ZrO_2 are first formed, desirably reacting to give the perovskite.[38] However, the AO may react with the CO_2 from the combusted organic components to give the carbonate.[38] Carbonate can endothermically decompose to CO_2 and AO [39,40], and the latter can react with ZrO_2 to give the $AZrO_3$ perovskite (e.g., A = Ba, Ca, or Sr).[38] The decomposition activation energies, and in practice, decomposition temperatures, increase with the atomic number ($CaCO_3 < SrCO_3 < BaCO_3$) and depend on the crystalline carbonate form, which can end up varying the physical-chemical characteristics and structural architecture of the aimed 3D perovskite.[41] In addition, phase transitions of the components and impurities may occur throughout the annealing. Local chemical composition or morphological inhomogeneities can be expected throughout the material, especially if carbonate is buried or surrounded by perovskite. Our group has observed similar findings for low-temperature annealing (≈600 C) of ZrO_2, leading to buried carbon, which paradoxically increases the intrinsic mechanical properties of ZrO_2.[42] A way forward is to compensate for composition inhomogeneities; an excess amount of A-rich components, such as an excess of Sr, Ba, or Ca, is sometimes used to compensate for carbonate formation.[38,43]

To our knowledge, the AM of 3D perovskite architectures with sub-micrometer sizes has not yet been presented. Hence, this work introduces a library of 3D architected alkaline-earth zirconates of (sub-)micrometer sizes additively manufactured using tailor-made photoresists suitable with the TPL. The

WILEY-VCH

3D-printed organic-inorganic polymeric structures are thermally processed in the air at 1000 °C to eliminate the organic constituents and facilitate the formation of miniaturized replicas composed of, e.g., $BaZrO_3$, $CaZrO_3$, and $SrZrO_3$ microarchitectures, denoted hereafter BZO, CZO, and SZO. The 3D ceramic microarchitectures and reference powders obtained from photoresists cured in bulk are investigated morphologically, structurally, and chemically. Insights into the optical properties of 3D printed architectures are provided using cathodoluminescence and wide-field photoluminescence emission to estimate the lifetime rate and defects in $BaZrO_3$, $CaZrO_3$, and $SrZrO_3$. The freedom and integrability of 3D structuring can aid the accomplishment of ceramic structures composed of multiple elements, benefiting from TPL. From the AM scope, the results can pave the path for fabricating larger alkaline-perovskite architectures using conventional printing techniques, e.g., stereolithography and digital light processing.

2. Results and discussion

2.1. Additive manufacturing of BZO, CZO, and SZO architectures

The freedom of manufacturing a 3D perovskite library *via* TPL is showcased with different architectures. TPL photoresins are a key component that enables direct writing of the alkaline-earth perovskites (Figure 1). The process commences with the preparation of the photoresists. The photoresists are prepared by dissolving zirconium acrylate (ZrA) and the respective alkaline-earth metal component, such as barium acrylate (BA), calcium methacrylate hydrate (CMH), or strontium acrylate hydrate (SAH) in dimethylsulfoxide (DMSO), methanol (MeOH) and acrylic acid (AA). The agents are combined with a crosslinker, pentaerythritol triacrylate (PETA), TPL photoinitiator, 7-Diethylamino-3-thenoylcoumarin (DETC), and a small volume of dichloromethane (DCM) (Figure 1 (a)). Upon complete dissolution, DCM and MeOH are removed under reduced pressure. The as-prepared

WILEY-VCH

resin is an orange-yellow mixture. Next, a photoresist droplet is cast onto a glass cover slide (Ø30 mm) and enclosed between two Kapton® tape spacer ribbons, onto which a Si chip (8 x 8 mm) is placed. Underside, immersion oil is applied, and the substrate is mounted into a holder of a commercial TPL 3D printer (Photonic Professional GT, Nanoscribe) in a reflection configuration. The pre-ceramic 3D architectures (metal-containing polymers) are printed on Si dice and developed in DMSO and MeOH to clear away the non-polymerized photoresist (Figure 1 (b)). The structures are dried to remove traces of solvents, placed in the chamber oven, and annealed in atmospheric air at 1000 °C for 5 hours. The 1°C/min ramp to 500 °C and 2°C/min ramp to the target temperature is applied to facilitate the combustion of organic constituents and the formation of metal grains, which are oxidized to yield metal oxides corresponding to the precursors used. The metal oxides mostly react to yield perovskites, though side-products may form (Figure 1 (d). For additional insights, readers are referred to the Supporting Information (Sections S2 – S5). A perovskite miniature replica of pre-polymeric structures is obtained (Figure 1 (c)). UV-cured photoresists are annealed under the same conditions to obtain powder-like perovskite as reference powders. Depending on the photoresin composition, the BZO, CZO, and SZO can be obtained.
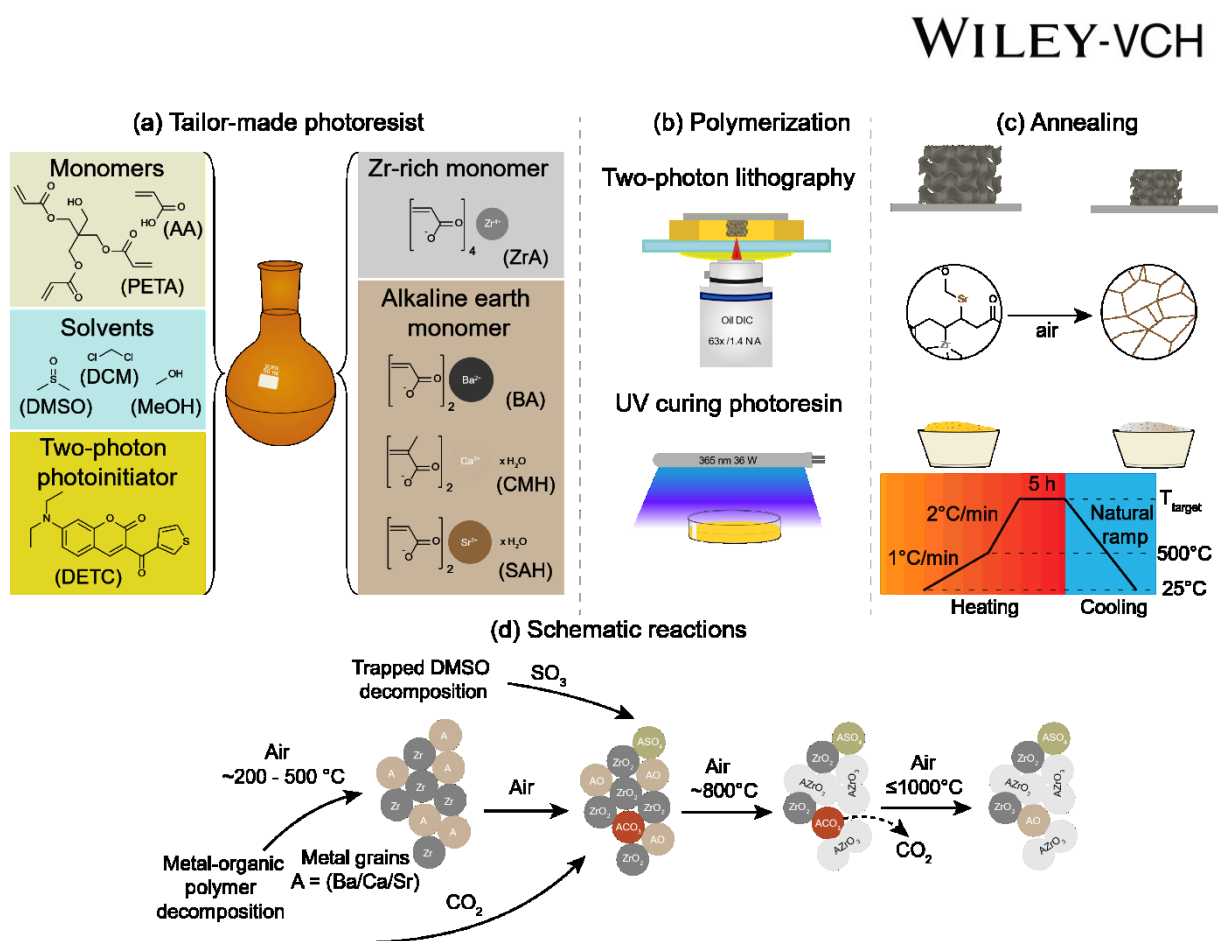
Figure 1. Additive manufacturing of BZO, CZO, and SZO 3D microarchitectures via TPL: (a) Tailor-made photoresists combining ZrA, AA, PETA, and DETC dissolved in DMSO, MeOH, and DCM with BA, CMH, or SAH. (b) 3D printing of the pre-ceramic 3D architectures (metal-containing polymers) on Si substrates using tailor-made photoresists or bulk using UV light. (c) Annealing of the pre-ceramic 3D architectures and UV-cured photoresists to obtain miniaturized perovskite replicas and reference powders at 1°C/min ramp to 500 °C, and 2°C/min to the target temperature (T_{target} = 600, 700, 800, 900, or 1000 °C) with cooling at the natural ramp. (d) Schematic representation of reactions – decomposition of metal-organic polymer yielding grains of Zr and alkaline-earth metal (A = Ba/Ca/Sr), which oxidize to the corresponding metal oxides – ZrO_2 or AO. The decomposition of organic constituents yields CO_2, which can form carbonates (ACO_3), and SO_3 formed via the combustion of trapped DMSO can react with AO to give ASO_4. While ACO_3 will likely decompose at 600 – 1000 °C, more stable ASO_4 will likely remain.

Scanning Electron Microscopy (SEM) micrographs of the ceramic architectures are shown for BZO and CZO in Figure 2 and SZO in Figure 3. SEM images of the corresponding pre-ceramic structures are presented (Figures S1 and S2, Supporting Information). SEM images of the reference powders

9

WILEY-VCH

annealed at the same temperature as the architectures are shown in Figure S3. For the BZO and CZO perovskites architectures in Figure 2, an isotropic shrinkage of ≈ 63% is observed upon annealing the pre-ceramic (Figure S1). After calcination at 1000 °C, the BZO C_{60} buckyball-inspired structure (buckyball) and sodalite-inspired structure remain of similar geometry to the pre-ceramic structure. Regardless of the buckyball or sodalite design, the beams of BZO 3D structures primarily comprise outward-located disc-shaped grains of submicrometer widths, lengths, and thickness in the range of tens of nanometers (Figures 2 (a' and b')). The angled positioning of grains and foreshortening renders the measurement of their sizes imprecise based on the image analysis; thus, approximate values are not given. Interestingly, the disc-shaped grains fused in the beams resemble the macroscale Saharan gypsum desert rose morphology.[44] Within the same architectures, smaller grains are positioned in the central parts and neighboring large crystal edges (see yellow arrow highlight). Sintered crystals are also observed in Figure 2 (a'). The preferential external situation of large disc-shaped crystals may be associated with heat transfer and local temperature inhomogeneities throughout the 3D architectures during annealing, as computed and experimentally investigated in mm-lengthscale ceramics.[45]

The CZO gyroid (Figure 2 (c)) comprises nanograins, more irregular than in BZO, with a width and length of approximately 100 - 200 nm. The zeolite sodalite-inspired architecture (Figure 2 d) has elongated oblong-like nanograins with approximate lengths of hundreds and widths of two hundred nanometers. A relation between the nanograin size and shape cannot yet be attributed to the architectural design. However, it can reasonably be related to the chemical composition of the perovskite architecture. For example, SZO (Figure 3) reveals larger crystals than BZO and CZO (Figure 2). Figure 2 (f – h) demonstrates the elemental distribution of (f) Ca, (g) Zr, and (h) O, homogeneously

allocated within the solid beams of the CZO sodalite-inspired architecture depicted in the SEM image

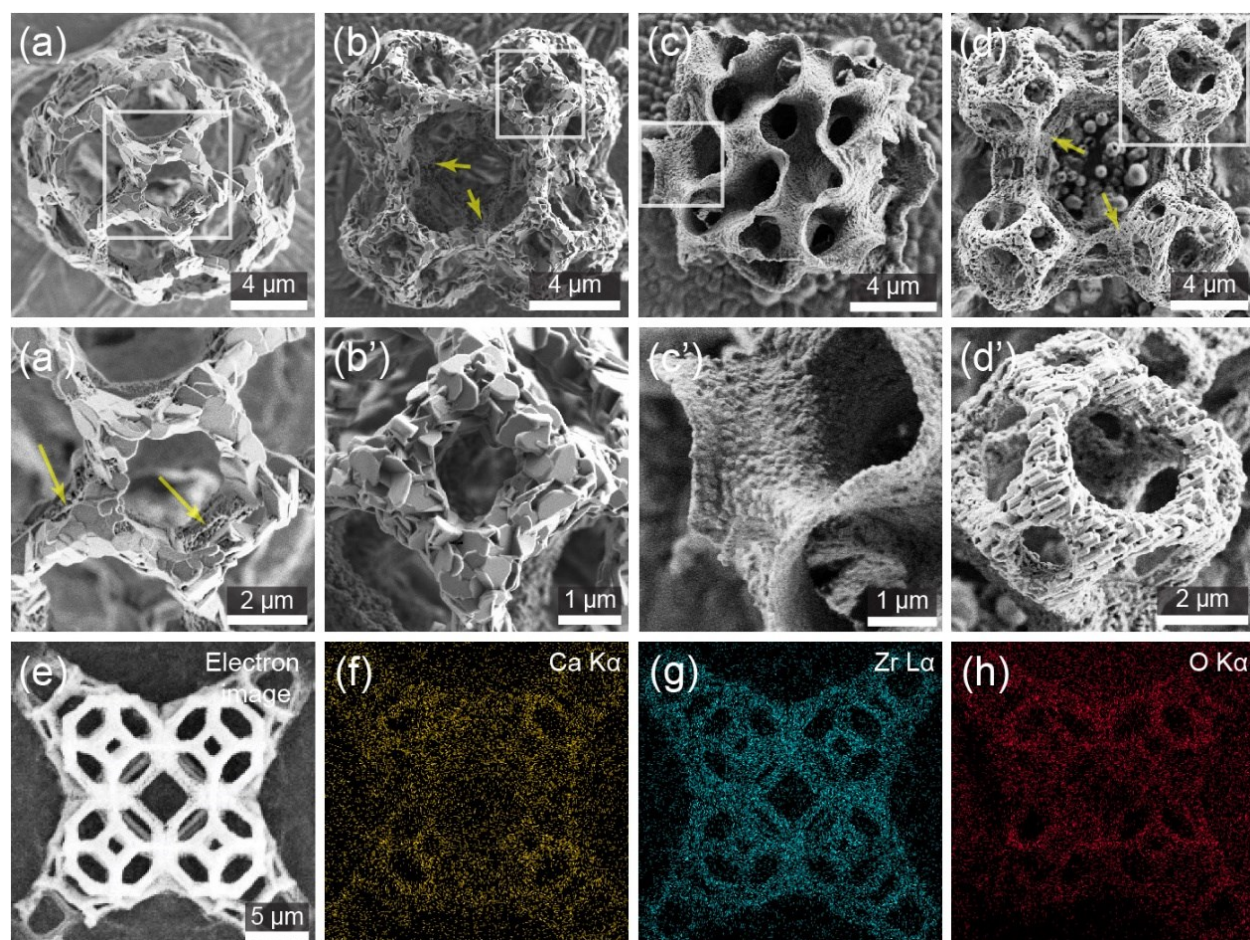(Figure 2 (e)); no areas appear to be deficient in one of these elements, no hotspots are found.

Figure 2. Morphological and chemical characteristics of the 3D BZO and CZO 3D architectures. SEM images of (a) BZO C$_{60}$ buckyball-inspired architecture, (b) BZO sodalite-inspired structure, (c) CZO gyroid, and (d) CZO zeolite sodalite-inspired structure. High-magnification SEM images (a'-d') of the areas indicated in the (a-d) micrographs. SEM-EDX mapping of the CZO sodalite-inspired structure presented in electron image (e), distribution of (f) Ca, (g) Zr, and (h) O.
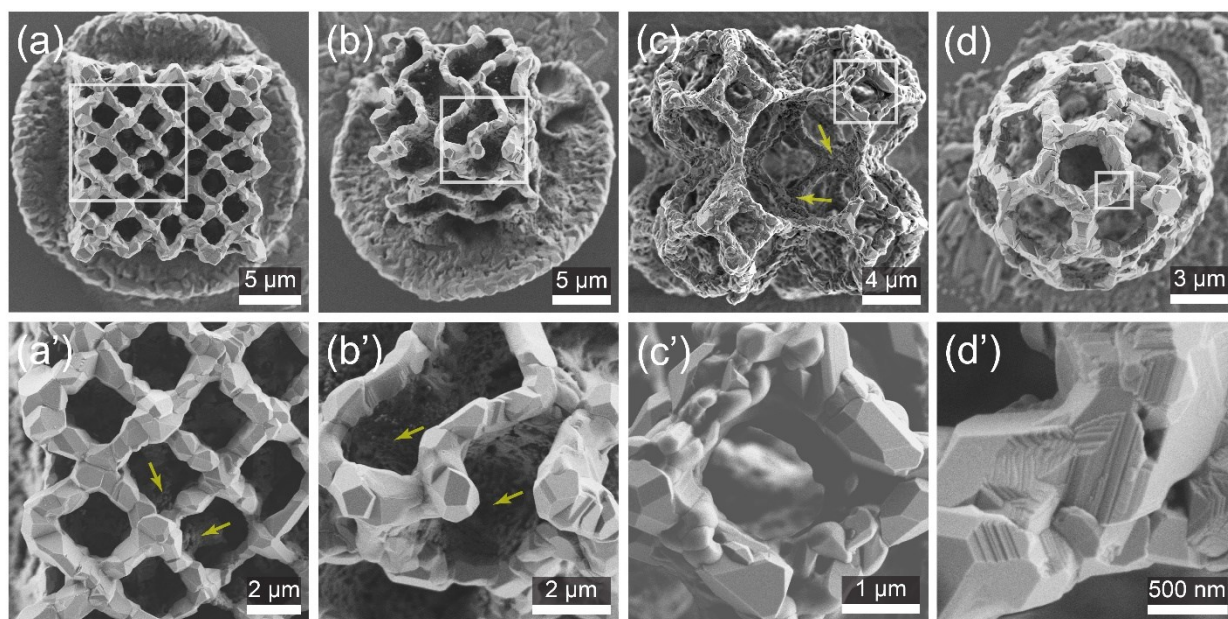
Figure 3. Morphological characterization of the additively manufactured SZO 3D microarchitectures. SEM images of (a) octet-truss lattice, (b) gyroid, (c) sodalite-inspired architecture, (d) C_{60} buckyball-inspired structure. High-magnification SEM images (a'-d') of the areas indicated in the (a-d) micrographs.

The SZO shows isotropic shrinkage similar to the other alkaline-earth zirconates. Larger grains of lengths and widths close to the micrometer have been observed. The sintering is pronounced at the grain boundaries and the microarchitecture edges (Figure 3). Additionally, nanometric grains are observed in the central areas of the octet-truss lattice and gyroid, as highlighted by the yellow arrows in Figures 3 (a) and (b)). Overall, SZO sharp-edge grains are smaller than in the gyroid and octet-truss lattice, and their size distribution is inhomogeneous. Even though the same annealing conditions are applied, these smaller grains are practically not noted in the more open architectures, like the sodalite-inspired structure (Figure 3 (c)). The effect can be related to the structure type, which due to thermal transport during annealing, might vary across the closely packed architectures (octet-truss lattice and gyroid). Similar observations to the zeolite-inspired architecture can be made for the buckyball (Figure 3 (d)), where multiple steps can be observed in the buckyball on the grain surface (Figure 3 (d')). These steps may be correlated with edge dislocations, in which vectors appear to align along the buckyball

WILEY-VCH

beams. These are very important observations from the crystal growth standpoint. The chemical composition, annealing treatment, and the ratio between the volume occupied by the material and air within the 3D architecture are factors that influence the crystal growth process. Tailoring such parameters, we can produce a perfect 3D crystal hypothetically.

From the image inspection in Figures 2 and 3, the largest grains are obtained for SZO and the smallest for CZO. For BZO and SZO, the crystal growth and morphology appear to depend on the geometry and composition of the 3D pre-ceramic microarchitectures. The structural integrity of the BZO and SZO octet-truss lattices is assessed with focused ion beam (FIB) tomography (Video S1 and S2, Supporting Information). The analysis reveals the inner polycrystalline microstructure. The SZO grains are densely packed, and voids are found within the BZO beams. In perspective, the future development of this TPL approach may open the possibility of growing crystals of specific chemical composition, morphology, size, or defects (i.e., point, line, or bulk defects) applicable for photocatalysis.[13,46,47] In retrospect, ultra-smooth crystals with fewer defects can facilitate light propagation with minimum losses, enabling the production of micro-optical components.

2.2. Structural characteristics of BZO, CZO, and SZO

BZO, CZO, and SZO reference powders (Figure 1) are synthesized from the corresponding tailor-made photoresins to limit potential impurities and control the microarchitecture chemical composition. The prepared UV-cured pre-ceramic photopolymers are pulverized and annealed in the crucibles at 600 °C, 700 °C, 800 °C, 900 °C, and 1000 °C for 5 hours to yield white BZO, CZO, and SZO powders.

The X-ray powder diffraction (XRD) measurements for the BZO (Figure S4, Section S2.1., Supporting Information) feature the reflections distinctive of cubic phase barium zirconate (c-BaZrO$_3$).[35] The

WILEY-VCH

main identified impurity is orthorhombic barium sulfate (o-BaSO4), and minor amounts of monoclinic zirconia (m-ZrO_2) are found. In CZO powder synthesized from the equimolar amount of Ca- and Zr-rich monomers, besides orthorhombic calcium zirconate (o-$CaZrO_3$), a significant amount of impurities, e.g., orthorhombic calcium sulfate (o-$CaSO_4$) and tetragonal zirconia (t-ZrO_2) are observed in Section S2.2., Supporting Information. The reference powders with Ca:Zr ratios 1:1, 1.1:1, 1.25:1, and 1.5:1 annealed at 1000 °C for 5 hours are studied to improve product quality (Figure S5, Supporting Information). The excess Ca is required to promote $CaZrO_3$ synthesis since the least impurities and the highest $CaZrO_3$ content are achieved for the Ca:Zr ratio of 1.5 to 1. The Ca concentration is not increased further due to the limited CMH solubility. The CZO (at 1.5 to 1 Ca: Zr ratio) powders synthesized from the UV-cured photoresists annealed at 600 °C, 700 °C, 800 °C, 900 °C, and 1000 °C for 5 hours are characterized (Figure S6, Supporting Information). At lower temperatures (600 °C, 700 °C, and 800 °C), large amounts of orthorhombic calcium sulfate (o-$CaSO_4$), calcium carbonate ($CaCO_3$), and tetragonal zirconia (t-ZrO_2) are found as impurities. The orthorhombic phase strontium zirconate (o-$SrZrO_3$) is identified for SZO (Figure S7, Supporting Information). Minor amounts of m-ZrO_2 and orthorhombic strontium sulfate (o-$SrSO_4$) are confirmed (Figure S7, Supporting Information). The ASO_4 (A = Ba, Ca, Sr) is related to the DMSO in the photopolymer (Figure 1).

In summary, XRD results for BZO show the characteristic features of c-$BaZrO_3$ upon annealing at 700 °C; the increased temperature improves crystallinity and reduces the general impurity content. In the case of CZO, at lower temperatures (600 °C, 700 °C, and 800 °C), large volumes of impurities are found, mostly suppressed after the treatment at 1000 °C. For SZO, reflections associated with o-$SrZrO_3$ are already detected for powders annealed at 600 °C, though a significant volume of impurities is found through 600 – 900 °C. The annealing of SZO at 1000 °C results in $SrZrO_3$ with a minor impure phase

14

WILEY-VCH

volume. The lattice parameters of BZO, CZO, and SZO annealed at 1000 °C agree with the literature (Supporting Information Table 1). On average, the treatment at 1000 °C yields the purest c-BaZrO$_3$, o-CaZrO$_3$, and o-SrZrO$_3$ perovskites (Figure S4, S6, and S7, Supporting Information); thus, it is selected as the annealing temperature for the 3D structures.

Complementary insights into impurities and surface composition of BZO, CZO, and SZO reference powders annealed for 5 hours at 1000 °C are provided using X-ray photoelectron spectroscopy (XPS). The general survey reveals the presence of Ba, Zr, O, C, and S in BZO (Figure S8 (a), Supporting Information). The analysis of BZO core regions confirms that BaZrO$_3$ is synthesized and BaSO$_4$ and BaCO$_3$ impurities are found (Figure S8 (b - f), Supporting Information). For CZO, the general survey proves the presence of Ca, Zr, O, C, and S (Figure S9 (a), Supporting Information). The dominant product is CaZrO$_3$, accompanied by CaCO$_3$ and traces of CaSO$_4$ (Figure S9 (b - f), Supporting Information). Significantly more CaCO$_3$ is found in CZO than in BZO and SZO. The analysis confirms that Sr, Zr, O, C, and S are present in SZO powder (Figure S10 (a), Supporting Information). The dominant component is SrZrO$_3$; similarly, SrCO$_3$ and SrSO$_4$ are detected as side-products (Figure S10 (b - f), Supporting Information). The species assigned with XPS are consistent with XRD analysis results.

Next, we analyze the chemical composition of the FIB-processed lamellae extracted from the BZO, CZO, and SZO microarchitectures. The results in Figure 4 are accompanied by SEM-EDX (Figures S11 – S14, Section S4, Supporting Information). The annular dark-field scanning transmission electron microscopy (ADF-STEM) images of lamellas are given in Figure 4 (a – c). The STEM-EDX mapping indicates the Ba, Zr, and O distribution throughout the BZO lamella in Figure 4 (a – a''') with visible Ba hotspots. The selected area electron diffraction (SAED) pattern indicates the mixing of ZrO$_2$ and BaZrO$_3$ phases (Figure S15 (a), Supporting Information). The findings are well aligned with previously

WILEY-VCH

discussed XRD and XPS results. Further, electron energy loss spectroscopy (EELS) shows the presence of edges from Zr, O, and Ba, all collected from a single grain (Figure S15 (d), Supporting Information). Next, the CZO is analyzed. The fragile nature of CZO made it difficult to prepare and handle a lamella; thus, higher-magnification images are provided of the representative region; the EDX maps confirm the homogenous allocation of Ca, Zr, and O within the sampled area. The corresponding SAED pattern indicates the presence of $CaZrO_3$ and ZrO_2 (Figure S15 (b), Supporting Information). For SZO, EDX confirms a more homogenous distribution of Sr, Zr, and O within the area of interest in Figure 4 (c – c'''), correlating with the SAED pattern dominated by reflections for $SrZrO_3$ (Figure S15 (c), Supporting Information). No discernible ZrO_2 rings have been found. However, some diffraction spots with values close to ZrO_2 are observed. Although there are some small inhomogeneities, forming mixed-phase products and segregation is a known phenomenon for alkaline-earth perovskites.[48,49] The local inhomogeneities in the composition of BZO, CZO, and SZO microarchitectures can be additionally related to the bulk character of the pre-ceramic beams, hindering the formation of stoichiometric product within their cores. In addition, STEM imaging reveals the nanoporosity within the nanoporous character within the core of the material (see Figure S16, supporting Information).
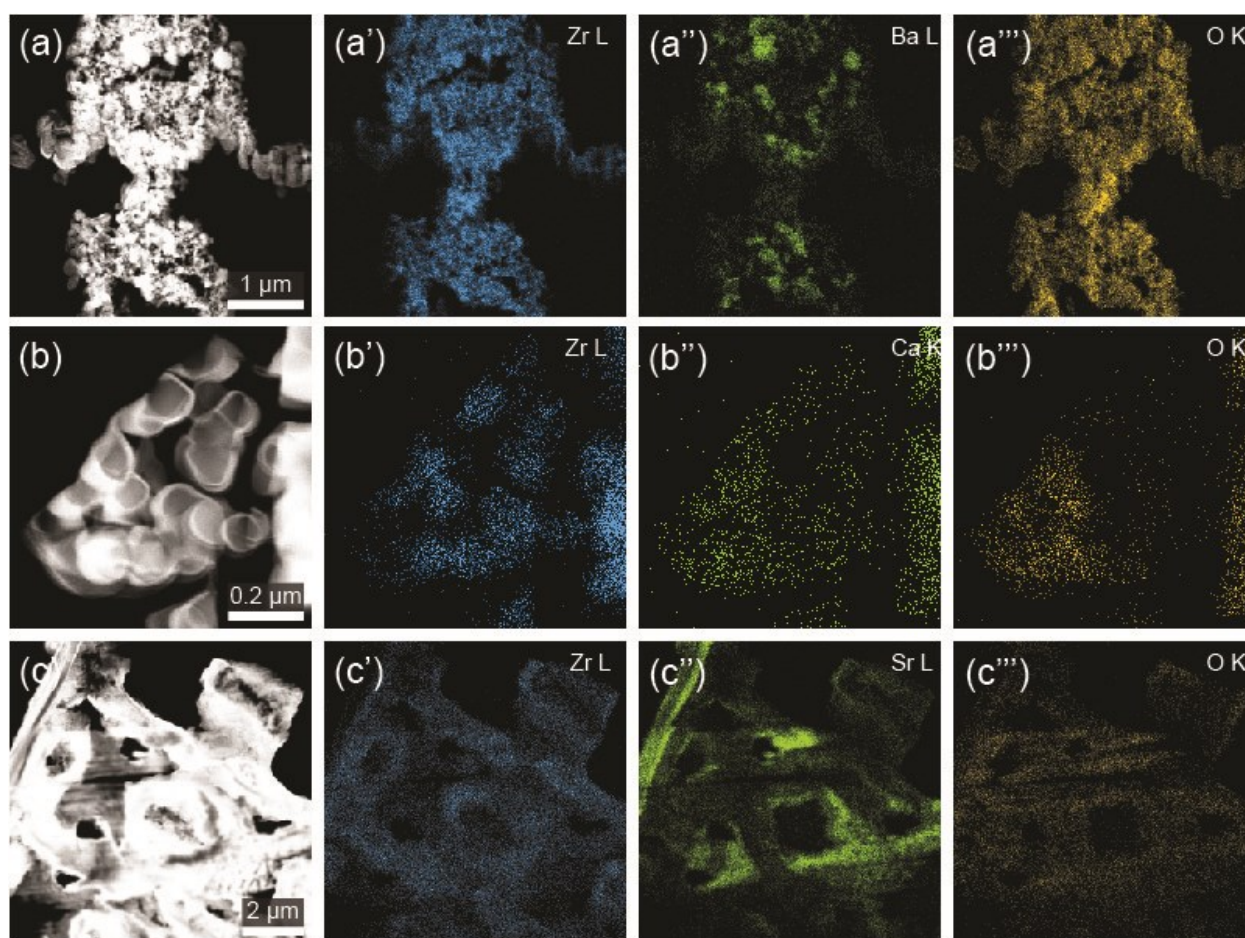
16

Figure 4. ADF-STEM images of BZO (a), CZO (b), and SZO (c) lamellas with corresponding EDX maps showing the distribution of Zr (a' – c'), alkaline-earth elements (a'' – c''), and O (a''' – c''') throughout the sampled areas.

2.3. Optical properties of BZO, CZO, and SZO

The optical properties of BZO, CZO, and SZO are evaluated. First, diffuse reflectance spectroscopy measurements are conducted for the BZO, CZO, and SZO powders (Section S7, Supporting Information). Using the Kubelka-Munk function and Tauc plot, 4.38 eV, 3.81 eV, and 4.31 eV, indirect transition band gaps are determined for BZO, CZO, and SZO, respectively (Figure S17, Supporting Information).[50] The estimated values agree with the literature. The BZO band gaps of 4.9 - 3.8 eV

17

WILEY-VCH

were reported for powders.[51,52] For reference, CZO 4.38 – 3.85 eV optical band gaps were measured, and band gaps of 4.1 - 3.3 eV were calculated.[53–55] SZO optical band gap values ranging from 5.5 eV to 3.5 eV were previously stated, depending on the synthesis method and morphology.[13,56,57] The band gaps of zirconates can be altered by the defects, i.e., oxygen vacancies, strain, and lattice mismatches.[55,58] Therefore, the nature of some defects is unraveled optically. Access to interrogate BZO, CZO, and SZO microarchitectures is nontrivial. First, cathodoluminescence (CL) measurements provide insights into the point defects and associated emissions. The CL spectra are deconvoluted into the peaks corresponding to defect-related emissions (Figures 5 (a-c)). The corresponding panchromatic SEM-CL images resenting the emissions from the 3D microarchitectures are shown (Figure 5 (a'' – c'')). CL spectra for BZO, CZO, and SZO reference powders are presented in Figure S18, Supporting Information for comparison. During peak-fitting of Gaussian components, 0.35 eV full width at half maximum (FWHM) is set. FWHM manifests a homogenous and inhomogeneous widening of line widths related to electronic transitions. The coupling between electrons and phonons within perfect crystals results in homogenous peak widening, illustrated with the Lorentzian profile. The disorder, *i.e.*, impurities, vacancies, or anti-site defects, contributes to the inhomogeneous peak widening, portrayed with the Gaussian profile.[59,60]
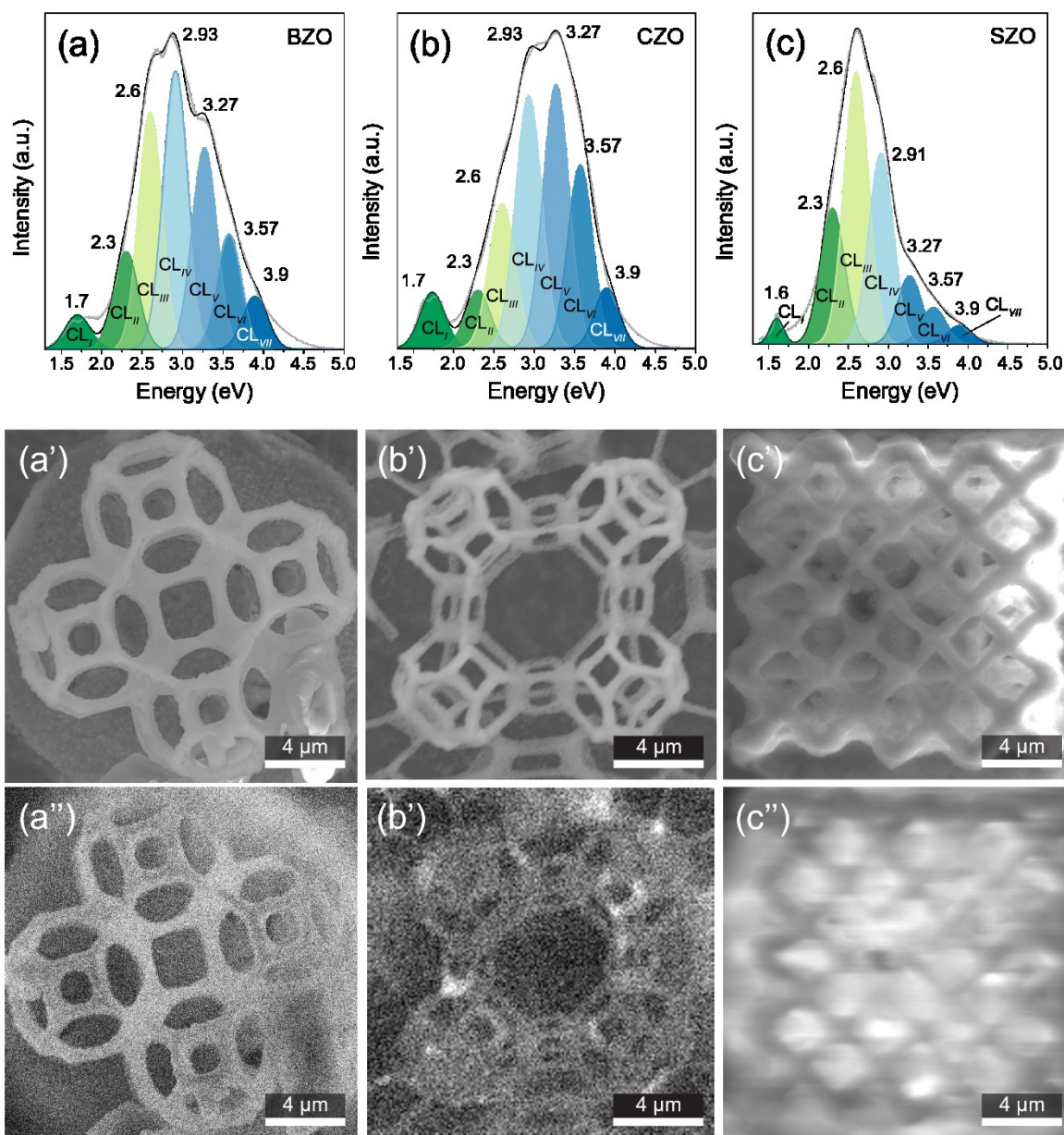
WILEY-VCH

Figure 5. Deconvoluted CL spectra collected from the (a) sodalite-inspired BZO, (b) zeolite sodalite-inspired CZO microarchitectures, and (c) octet-truss lattice SZO, and corresponding SEM (a' – c') and panchromatic SEM-CL (a'' – c'') images.

First, the CL spectrum recorded for BZO microarchitectures is discussed. The Gaussian components are fitted at 1.7 eV (CL$_I$), 2.3 eV (CL$_{II}$), 2.6 eV (CL$_{III}$), 2.93 eV (CL$_{IV}$), 3.27 eV (CL$_V$), 3.57 eV (CL$_{VI}$), and 3.9

19

WILEY-VCH

eV (CL$_{VII}$). The spectrum is dominated by CL$_{IV}$ contribution, followed by high-intensity CL$_{III}$ and CL$_V$ signals. The intensity of medium-intensity CL$_{II}$ and CL$_V$ peaks is comparable, while CL$_I$ and CL$_{VII}$ are relatively weak. The observed broad-range emissions stem from a multiphonon, multilevel process, including various relaxation pathways.[61–63] The spectrum is a combination of emissions correlating with structural order-disorder of ZrO$_5$ and ZrO$_6$ clusters, distortion, dangling bonds, oxygen vacancies (V$_O$), singly-ionized V$_O$ (V$_O^{\bullet}$), or disorder in the BaO$_{12}$ and ZrO$_6$ network.[51,62–65] The assignments of particular peaks in literature are often divergent and may differ depending on the synthesis method, particle morphology, size (*e.g.*, nanometric or micrometric size), or crystallinity.[62] The emission around 1.6 - 1.7 eV was previously assigned to the V$_O$ in HfO$_2$, Hf^{4+}, or other transition elements, which trace amounts are often found in ZrO$_2$.[66,67] Cavalcante *et al*. used electron paramagnetic resonance (EPR) measurements to correlate the 2.3 eV emission with V$_O^{\bullet}$ associated with [ZrO$_5$] clusters.[51] The 2.6 eV emissions were reported to stem from the structural order-disorder governed by [ZrO$_5$] and [ZrO$_6$] clusters or [BaO$_{12}$] sites.[61,64,68] The 2.9 eV emissions correlate with the V$_O$, or singly-ionized V$_O$ (V$_O^{\bullet}$) associated with [ZrO$_5$] clusters.[62,69] The weak UV and violet emissions (3.9 eV, 3.57 eV, and 3.27 eV) correlate with shallow trap states.[70] Conversely, the peaks around 3.29 – 3.44 eV were previously assigned to free exciton recombination.[64,71] Similar emissions have been observed for BZO reference powders in Figure S18 (a), Supporting Information. Interestingly, the 2.3 and 2.6 eV emissions are lower for the powder references than the 3D microarchitectures, indicating a lower degree of disorder for the powder samples. Additionally, BZO powder reveals the loss of the 3.9 eV emission previously assigned to shallow trap states. Besides the spatial organization offered by 3D printing, which can enable the control of (photo)chemical reaction performance[72],[73] or light-matter interaction in optics and photonics.[22] Defective and disordered BZO 3D microarchitectures can be treated as oxygen-

WILEY-VCH

deficient systems, which hold important applications in electrochemistry. This is the case with lithium-ion batteries, where our BZO 3D microarchitectures might play a crucial role during anion-redox reactions.[74],[75]

The CL spectrum collected from the CZO microarchitecture (Figure 5 (b)) is deconvoluted into seven peaks at 1.7 eV (CL_I), 2.3 eV (CL_{II}), 2.6 eV (CL_{III}), 2.93 eV (CL_{IV}), 3.27 eV (CL_V), 3.57 eV (CL_{VI}), and 3.9 eV (CL_{VII}). The CL_I, CL_{II}, and CL_{VII} peaks are very weak. The CL_{IV} and CL_V components dominate the spectrum, while CL_{III} and CL_{VI} are medium-intensity. The data regarding luminescent properties of CZO is limited; nonetheless, its emissions were previously associated with V_O, $V_O^{\cdot}$ and the distorted Ca and Zr networks, with the resulting $[CaO_7 \cdot V_O^{\cdot}]$, $[CaO_7 \cdot V_O^{\cdot\cdot}]$, $[ZrO_5 \cdot V_O^{\cdot}]$ and $[ZrO_5 \cdot V_O^{\cdot\cdot}]$ centers.[76,77] Certain resemblances of CL spectra of BZO and CZO are present, indicating potential similarities of defects to which the emissions correlate. Furthermore, the deconvolution of the SZO CL spectrum gives seven Gaussian components, ranging from long-wave UV to red. The peaks are found at 1.6 eV (CL_I), 2.3 eV (CL_{II}), 2.6 eV (CL_{III}), 2.91 eV (CL_{IV}), 3.27 eV (CL_V), 3.57 eV (CL_{VI}), and 3.9 eV (CL_{VII}). The weak UV and violet emissions at CL_{VII} − CL_{III} are associated with shallow defects within E_g, such as $[SrO_{11} \cdot V_O^{\bullet}]$ and $[SrO_{11} \cdot V_O^{\bullet\bullet}]$ clusters.[78–80] These also imply the off-stoichiometric material character.[81] The emissions ranging from green to red, e.g., CL_I and CL_{II}, correlate with the deep E_g defects, such as $[ZrO_5 \cdot V_O^{\bullet}]$ and $[ZrO_5 \cdot V_O^{\bullet\bullet}]$.[78–80] Similar to BZO reference powders, CZO and SZO (Figure S18 (b), and Figure S18 (c), Supporting Information), the 2.3 and 2.6 eV emissions are reduced for the powder references than the 3D microarchitectures. Additionally, CZO and SZO powder reveal the loss of the 3.9 eV emission. Those characteristics are of importance in the field of reaction chemistry, such as photocatalysis.[72],[73] Although BZO, CZO, and SZO reveal optically the presence of oxygen deficiencies, the optical response is attributed to local inhomogeneities in our alkaline-perovskite microarchitectures, we can expect

WILEY-VCH

that longer annealing times to reduce background emissions from defects for the production of refractive index ceramics in micro-optics.[8],[82] Our group has observed similar findings for low-temperature annealing (≈600 C) of denser ZrO_2 ceramics,[24] which could have caused the buried of carbon or non-stochiometric components,[42] as could be the case for non-stoichiometric BZO, CZO, and SZO species.

Next, we evaluate the wide-field photoluminescence (PL) emission to estimate the lifetime rate of defects in the alkali-earth perovskite printed architectures. For BZO, the local emission maxima are recorded at approximately 543 nm for excitation at 450 nm in Figure S19 (a). In the case of CZO, excitation at 450 nm in emissions with local maxima around 543 nm (Figure S19 (b)). For SZO, the highest PL emission intensity is observed at around 571 nm upon excitation at 450 nm (Figure S19 (c)). The registered PL signals are excited at relatively low energies due to the availability of the optical systems. The registered PL spectra are limited to the signals corresponding to the cathodoluminescence emissions assigned to the CL_I, CL_{II}, CL_{III}, and CL_{IV} peaks associated with Vo and intrinsic metal-oxygen coordinated centers.

The photoluminescence (PL) decay rate histograms are obtained through time-correlated single-photon counting (TCSPC) measurements to understand the lifetime of excited states in alkaline-earth perovskites. The BZO, CZO, and SZO samples are excited with a 450 nm wide-field laser beam emitted by a super-continuum laser using an inverted fluorescence microscope with a 20x objective. The PL emission is collected and focused onto a single photon avalanche diode coupled to a time-resolved photon counting module, with a 2.5 μm field of view and ~ 200 ps instrument response function (IRF) temporal width using the measured fluorescence intensity at a specific time ($I_{(t)}$), the decay

22

WILEY-VCH

histograms are fitted by convoluting the IRF with a sum of exponential functions to estimate fluorescence decay times (τ_n), shown in Equation 1:

$$I_{(t)} = \sum_n^N A_n e^{-\frac{t}{\tau_n}}$$ Equation (1)

The fitted normalized decay histograms for (a) BZO, (b) CZO with $N = 2$, and (c) SZO with $N = 3$ are presented in Figure 6. For BZO, the average photoluminescence lifetimes from 3 measurements are $\overline{t_1}$ = 0.29 ± 0.16 ns, $\overline{t_2}$ = 2.43 ± 0.58 ns. Similar excited-state and exciton lifetimes in BaZrO$_3$ were previously reported, and decay patterns imply that multiple processes participate in observed emissive exciton decay or radiative transitions.[83] Due to the noise, only a single conclusive spectrum is collected for CZO with estimated t_1= 0.13 ns and t_2 = 1.23 ns lifetimes. The 1.23 ns value was reported for CZO, correlated with oxygen vacancies (V$_O$).[76] In the case of SZO, the average of 4 measurements gives $\overline{t_1}$ = 0.08 ± 0.02 ns, $\overline{t_2}$ = 0.45 ± 0.03 ns, $\overline{t_3}$ = 1.89 ± 0.08 ns. The $\overline{t_1}$ value, significantly shorter than the IRF, is correlated to fast decay processes inside the material. Similar decay timescales were observed for SrTiO$_3$, which luminescence is not solely correlated with bulk V$_O$, but also with other unidentified intrinsic defects acting as radiative centers.[84] It is important to note that in Figure 6 (a-c), we observe a significant difference in the signal-to-noise ratio (SNR) comparing the three samples. These measurements have been conducted under identical conditions, highlighting the remarkable SNR exhibited by the SZO sample. Upon analyzing the raw data, the intensity of the SZO sample surpasses that of the BZO sample by a factor of 20 and the CZO sample by a factor of 40. This tendency also holds true in wide-field fluorescence images, further supporting the superiority of the SZO sample in excitation efficiency.
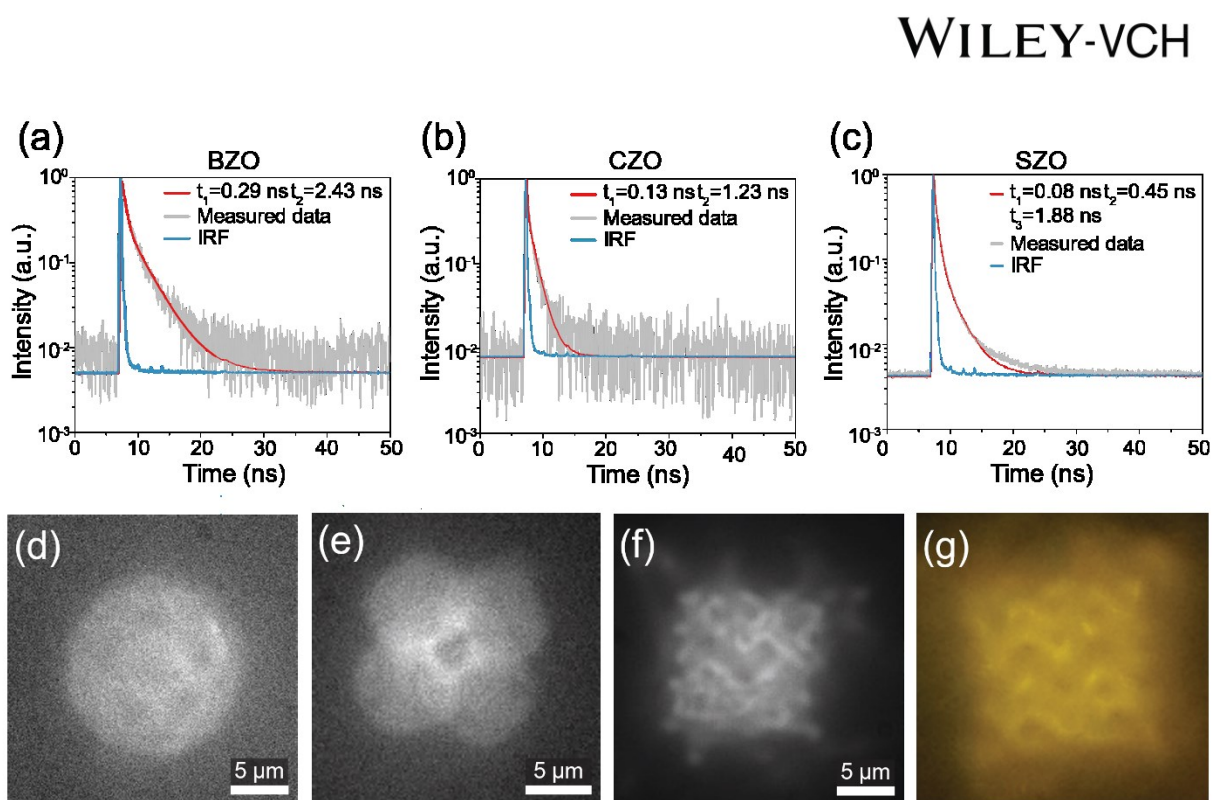
Figure 6. Normalized PL decay profiles upon 450 nm excitation for (a) BZO, (b) CZO, and (c) SZO microarchitectures; Wide-field fluorescence microscopy images of (d) BZO buckyball, (e) BZO sodalite-inspired architecture, and (f) SZO gyroid upon 488 nm excitation; (g) digital image from the microscope eye-piece presenting yellow emission from the SZO gyroid excited at 488 nm.

Top-view photoluminescence images showcasing the emission from the BZO buckyball, sodalite-inspired architecture, and SZO gyroid upon excitation at 488 nm are presented in Figure 6 (d - g). The corresponding stop-motion videos presenting z-stack acquisition are also presented (Video 1 - 3, Supporting Information). Figure 6 (g) gives a digital image from the microscope eye-piece showcasing defect-related yellow emission from the SZO gyroid excited at 488 nm. In addition, the photoluminescence (PL) emission spectra are recorded for the 3D BZO, CZO, and SZO microarchitectures using a wide field microscopy setup at 20 x magnification and 415 nm, 450 nm, or 488 nm excitation (Oxxius) (Figure S19, Supporting Information). The emission is filtered using a dichroic mirror with the matched fluorescence filter.

This article is protected by copyright. All rights reserved.

24

WILEY-VCH

3. Conclusion

Additive manufacturing of 3D-structured perovskite microarchitectures was achieved for the first time using two-photon lithography and tailor-made photoresins. Upon the annealing in the air, the 3D-printed pre-ceramic complex microarchitectures were transformed into the corresponding miniaturized perovskite replicas, isotropically shrunken by ≈ 63 %. The effects of the thermal treatment (5h at 600 °C, 700 °C, 800 °C, 900 °C, and 1000 °C) were studied with XRD. Gradual temperature increases result in the reduced content of impurities, mainly including corresponding sulfates and carbonates with traces of zirconia. Additional characterization with XPS was conducted, confirming the formation of perovskites and the presence of similar impurities on the surface. The synthesis of $BaZrO_3$, $CaZrO_3$, and $SrZrO_3$ was accomplished.

SEM imaging of BZO, CZO, and SZO microarchitectures allowed us to observe crystallites of significantly different grain morphologies. FIB tomography revealed the structural integrity of the representative 3D microarchitectures and enabled the assessment of the homogeneous distribution of Ba/Ca/Sr, Zr, and O throughout the extracted lamellae with EDX. The analysis of BZO, CZO, and SZO lamellae with STEM confirms the formation of $BaZrO_3$, $CaZrO_3$, and $SrZrO_3$. However, a mixed state with ZrO_2 is commonly observed, also evidenced with EDX maps. Visible-range emissions from the manufactured BZO, CZO, and SZO 3D microarchitectures were observed with CL and PL, correlated with various lattice defects, structural order-disorder, and trap states. The PL decay histograms are obtained through TCSPC measurements, enabling the determination of the photoluminescence lifetimes, similar to literature values of $BaZrO_3$, $CaZrO_3$, and $SrZrO_3$.

WILEY-VCH

From a broad perspective, the presented methodology permits the AM of complex 3D-structured mixed oxides, whose chemical composition can be tuned. Our work is the first step toward fabricating dimensionally refined perovskite microarchitectures, which are significant in photonics, optoelectronics, sensing, and (photo)catalysis.

4. Experimental procedure

4.1. Materials

Barium acrylate (95%), calcium methacrylate hydrate (95%), and strontium acrylate hydrate (90.5%) were ordered from TCI Europe NV, abcr GmbH, and Gelest, respectively. Isopropanol (ACS reagent, ≥99.5%), methanol (99.9 %), pentaerythritol triacrylate (technical grade), and zirconium acrylate were obtained from Sigma-Aldrich. Acrylic acid (99%, stabilized with ca 200ppm 4-methoxyphenol), dichloromethane (99.9%), and dimethyl sulfoxide (>99%) were acquired from Alfa Aesar. 7-Diethylamino-3-thenoylcoumarin (97%) was acquired from J&K Scientific. All agents were used as received.

4.2. Organic-inorganic photoresists for two-photon lithography

TPL-compatible photoresins permitting printing precursor photopolymers of BZO, CZO, and SZO suitable for two-photon polymerization (Figure S20 and Figure S21, Supporting Information) with molar absorptivity of 8.78 M^{-1} cm^{-1} were prepared and handled using amber glassware in a yellow-light environment. Acrylic acid (150 mg) was poured into a round bottom flask containing combinations of metal-organic monomers. A fixed amount of zirconium acrylate (37.5 mg) was mixed with barium acrylate (29.5 mg) or strontium acrylate hydrate (27.4 mg), respectively. The zirconium

acrylate and calcium methacrylate ratios were precisely adjusted to formulate the recipes yielding the CZO with low side-product quantities (e.g., 37.5 mg ZrA, and 22.4 mg CMH for 1:1 Zr:Ca ratio). To this end, samples with a stoichiometric Zr:Ca ratio and different non-stoichiometric ratios were prepared (i.e., 1:1; 1: 1.1; 1:1.25; 1:1.5). To the mixtures, methanol (2 g) and DMSO (500 mg) were added and agitated using a rotary evaporator operated under ambient pressure (40 ºC/180 rpm/60 min). After the dissolution of metallic salts, the organic monomer (300 mg), PETA, was added to the flask, and the mixing continued for 30 min. Afterward, the photoinitiator, DETC (23 mg), and DCM (200 mg) were added. The solution was mixed for 15 minutes, and later, the pressure was reduced for complete evaporation of MeOH and DCM (40ºC/180 rpm/45 min). The freshly prepared photoresin was used in a TPL process directly.

4.3. Two-photon lithography and UV curing

Pre-ceramic architectures (metal-containing polymers) were written on substrates using a commercially available TPL system with an inverse configuration (Photonic GT, Nanoscribe GmbH). The photoresins were drop cast onto glass cover slides (Ø 30 mm) and enclosed between two Kapton® tape strips as spacers, on which Si chips (8 x 8 mm) were placed. The printing setup consists of an oil-immersion configuration with a 63x objective lens with numerical aperture NA=1.4. The system was operated using reflection mode at an average laser power of 23.5 mW and 1 mm s^{-1} scan speed. The peak laser intensity was estimated to be close to 9.64 TW/cm^2 for these conditions. The two-photon polymerization (TPP) dose was estimated using Equation 2.[79] The estimated TPP dose for each pre-ceramic resin was 53.84 J/cm^2. Furthermore, we have estimated that the standard laser source has a central wavelength (λ) at a 780 nm repetition rate 80 MHz (f_{rep}), pulse width 100 fs (τ_L), maximum output power 140 mW, and peak power 25 kW. For high-resolution 3D printing, the focal spot size can

WILEY-VCH

be described through the optical lateral resolution (ω_0) and axial resolution (d_x). ω_0 and d_x are shown in Equation 3 and Equation 4. In this case, ω_0 was 278.6 nm, and d_x was 298 nm.[80]

$$D = f_{rep}\tau_L\sqrt{\frac{2}{\pi}}\frac{P_t}{\omega_0\, v} \qquad\qquad\qquad \text{Equation (2)}$$

$$\omega_0 = \frac{\lambda}{2\,NA} \qquad\qquad\qquad \text{Equation (3)}$$

$$d_x = \frac{\lambda}{(NA)^2} \qquad\qquad\qquad \text{Equation (4)}$$

After conditioning our Nanoscribe system to the previous conditions and printing, the structures were first immersed in DMSO for 2 min and then in MeOH for 5 min to develop to be finally dried with a gentle nitrogen stream. The portions of freshly prepared photoresins non-used during printing were poured into Petri dishes and irradiated with a 36 W halogen UV lamp (365 nm, EBN001, Esperanza) to prepare reference powders in bulk. After ten cycles of 60 min irradiation, the obtained metal-organic photopolymers were ground in an agate mortar and placed into crucibles. The printed structures and UV-cured samples were dried with a nitrogen stream and stored in an oven overnight (ED 23, Binder GmbH) at 80 °C to evaporate traces of DMSO.

4.4. Annealing

The 3D-printed microarchitectures and reference powders were placed in open-cap ceramic crucibles to remove the organic constituents from the pre-ceramic polymer and later annealed in an air chamber oven (LH 15/12, Nabertherm). The heating program consisted of a slow heating ramp step (1 °C min^{-1}) to reach 500 °C, followed by a second stage (2 °C min^{-1}) to reach the target temperature

WILEY-VCH

(600 °C, 700 °C, 800 °C, 900 °C, or 1000 °C, respectively. The samples were annealed for 5 h and then cooled to room temperature at a natural rate.

4.5. Characterization

X-Ray Powder Diffraction (XRD): The influence of the annealing conditions on the crystallinity of the yielded powders was characterized using X-ray Powder Diffraction (XRD). The powdered samples of the UV-cured annealed photoresins were placed on a zero-diffraction substrate and analyzed using an X-ray diffractometer (D2 Phaser, Bruker). The data was acquired within a 20 - 80° 2θ scan range using a LynxEye detector and Cu-Kα source radiation (30 kV, 10 mA). CrystalSleuth software was used for baseline correction of data.

Scanning Electron Microscopy (SEM): The high-resolution images of the printed 3D structures and reference powders were registered using High-Efficiency Electron (HE-SE2) and Inlens detector of the Carl Zeiss, Merlin AURIGA CrossBeam workstation operated at 1.5 kV acceleration voltage.

Scanning Transmission Electron Microscopy (STEM): The electron microscopy and chemical analysis were performed in a JEOL ARM-CF Cs corrected microscope, operated at 200 kV, and equipped with an SSD Jeol EDX and a GIF Quantum (Gatan) Dual EELS spectrometer.

Focused Ion Beam (FIB) Processing and FIB tomography: The Thermo Scientific Helios 5 UX DualBeam workstation was used to prepare lamellae. The sections of 3D-printed structures were milled using a Ga source, welded to the Cu grid with W, Pt, and C, to be finally thinned and polished using low-energy ions (W, Si). The FIB tomography of BZO and SZO lamellae was performed using Auto Slice & View 4 software; the secondary electron images were recorded at 2 kV acceleration voltage and

approximately 100 nm slice thickness. In total, 150 frames were recorded for BZO and 74 for SZO. In addition, SEM and STEM images were acquired at 10 kV acceleration voltage.

Energy-Dispersive Spectroscopy (EDX): The energy-dispersive spectra were recorded using the EDX attachment to the FIB workstation. The EDX maps were generated using Thermo Scientific Pathfinder X-ray Microanalysis Software. The single pixel size is 100.1 nm; the images were upscaled for display.

Cathodoluminescence (CL): CL measurements were conducted at room temperature with a JEOL JIB-4500 SEM using a Gatan MonoCl4 detector operated at 15 kV acceleration voltage. ***Reflectance Spectroscopy (UV-Vis DRS)***: The BZO, CZO, and SZO reference powders were dispersed in isopropanol and cast on glass slides dropwise. After solvent evaporation, uniform films were obtained, which adhered to the substrate when stored vertically. The UV-Vis DRS spectra were collected using a Lambda 950 S (Perkin Elmer) spectrometer using a 150 mm InGaAs integrating sphere (Perkin Elmer) and a focusing lens (Melles Griot). The photomultiplier tube and InGaAs detector slits were 4 and 2 nm. The deuterium lamp was changed to tungsten at 319 nm. As a reference, Spectralon® (Labsphere) reflectance standard was used.

Photoluminescence (PL): The sample was positioned facing the objective (i.e., with the substrate behind the printed structures) and mounted in the sample holder by attaching the substrate to a glass coverslip (170 μm thickness, 25mm diameter) with double-sided adhesive tape. The decay histograms were obtained through time-correlated single-photon counting (TCSPC) measurements. The samples were placed on an inverted fluorescence microscope with a 20x objective and excited with a wide-field laser beam emitted by a super-continuum laser (SuperK Extreme EXB-6, NKT) tuned at 450 nm (FWHM ~ 10 nm). The resulting PL was collected with the same objective and focused onto a SPAD

(single photon avalanche diode, PDM-Red, Micro Photon Devices) coupled to a time-resolved photon counting module (HydraHarp400, PicoQuant). The field of view of the detector is 2.5 µm, and its instrument response function (IRF) has a temporal width of ~ 200 ps. The decay histograms were fitted, convoluting the IRF with a sum of exponential functions: $I_{(t)} = \sum_n^N A_n e^{-\frac{t}{\tau_n}}$, where τ_n is the fluorescence decay of the nth component.

Wide field fluorescence microscopy:

The sample was positioned facing the objective (i.e., with the substrate behind the printed structures) and mounted in the sample holder by attaching the substrate to a glass coverslip (170 µm thickness, 25mm diameter) with double-sided adhesive tape. No immersion oil was used. A 60x 1.40 NA (Nikon, Plan Apo lambda) objective was mounted on a Nikon Ti Eclipse 2 microscope body. The excitation was generated using a 488 nm laser (Oxxius, LBX-488-100) with 200 W/cm² irradiance. The emission was separated from the excitation and filtered by a quad-based 405/488/561/647 nm dichroic mirror with the matched fluorescence filter (Semrock). The detection path consisted of an afocal to adapt the magnification and an sCMOS camera (Photometrics Prime 95B). The exposure is set to 30 ms, and the pixel size in the object plane is 110 nm. The 3D images were acquired by capturing z-stacks. The axial displacement was achieved using a piezoelectric nanopositioner (PI), and one 300 ms exposure frame was recorded each 500 nm.

X-ray Photoelectron Spectroscopy (XPS)

The XPS analysis of the BZO, CZO, and SZO reference powders was conducted with a scanning XPS/HAXPES microprobe (PHI Quantes). An Al Kα source (1486.6 eV; 25 W, 15 kV) of 100 µm spot size was used. The general survey and core spectra were collected using 280 eV and 112 pass energies,

WILEY-VCH

with 1 eV and 0.1 eV steps, respectively. The synthetic Voigt peaks were generated using the CasaXPS package to deconvolute the spectra; Tougaard and Shirley background types were used. The core spectra are calibrated to the position of the aliphatic carbon peak (C-C, C-H) at 284.8 eV.

Supporting Information

Supporting Information is available from the Wiley Online Library or from the author.

Conflict of Interest

The authors declare no conflict of interest.

WILEY-VCH

References

[1]   Z. Zeng, Y. Xu, Z. Zhang, Z. Gao, M. Luo, Z. Yin, C. Zhang, J. Xu, B. Huang, F. Luo, Y. Du, C. Yan, *Chem. Soc. Rev.* **2020**, *49*, 1109.

[2]   M. Johnsson, P. Lemmens, in *Handb. Magn. Adv. Magn. Mater.* (Ed.: A.I. and H.K. H. Kronmüller, S. Parkin, M. Coey), John Wiley & Sons, Ltd, Chichester, UK, **2007**.

[3]   M. A. Peña, J. L. G. Fierro, *Chem. Rev.* **2001**, *101*, 1981.

[4]   P. Kanhere, Z. Chen, *Molecules* **2014**, *19*, 19995.

[5]   A. Kumar, A. Kumar, V. Krishnan, *ACS Catal.* **2020**, *10*, 10253.

[6]   N. N. Greenwood, A. Earnshaw, in *Chem. Elem.* (Eds.: N.N. Greenwood, A. Earnshaw), Butterworth-Heinemann, Oxford, United Kingdom, **1997**, pp. 107–138.

[7]   S. A. Cotton, *Annu. Reports Prog. Chem. - Sect. A* **1997**, *93*, 143.

[8]   G. Balčas, M. Malinauskas, M. Farsari, S. Juodkazis, *Adv. Funct. Mater.* **2023**, 2215230.

[9]   S. Parida, S. K. Rout, V. Subramanian, P. K. Barhai, N. Gupta, V. R. Gupta, *J. Alloys Compd.* **2012**, *528*, 126.

[10]   M. H. Lin, M. C. Wu, C. Y. Huang, C. H. Lin, T. Y. Tseng, *J. Phys. D. Appl. Phys.* **2010**, *43*, DOI 10.1088/0022-3727/43/29/295404.

[11]   S. Parida, S. K. Rout, L. S. Cavalcante, E. Sinha, M. S. Li, V. Subramanian, N. Gupta, V. R. Gupta, J. A. Varela, E. Longo, *Ceram. Int.* **2012**, *38*, 2129.

[12]   A. K. Kunti, N. Patra, R. A. Harris, S. K. Sharma, D. Bhattacharyya, S. N. Jha, H. C. Swart, *Inorg. Chem. Front.* **2021**, *8*, 821.

[13]   A. M. Huerta-Flores, F. Ruiz-Zepeda, C. Eyovge, J. P. Winczewski, M. Vandichel, M. Gaberšček, N. D. Boscher, H. J. G. E. Gardeniers, L. M. Torres-Martínez, A. Susarrey-Arce, *ACS Appl. Mater. Interfaces* **2022**, *14*, 31767.

WILEY-VCH

[14]   Z. Kang, B. Yu, S. Fu, D. Li, X. Zhang, Z. Qian, Z. Zhong, B. Yu, H. Ding, Y. Zhu, J. Huang, *Appl. Mater. Today* **2019**, *16*, 132.

[15]   H. Cui, R. Hensleigh, D. Yao, D. Maurya, P. Kumar, M. G. Kang, S. Priya, X. (Rayne) Zheng, *Nat. Mater.* **2019**, *18*, 234.

[16]   V. V. Vogler-Neuling, R. Savo, D. Pohl, N. R. Hendricks, L. Lang, M. Timofeeva, B. Schneider, F. U. Richter, F. Timpu, S. Monneret, F. Starsich, R. Grange, *Phys. Status Solidi Basic Res.* **2020**, *257*, DOI 10.1002/pssb.201900755.

[17]   H. Chen, J. Wang, S. Peng, D. Liu, W. Yan, X. Shang, B. Zhang, Y. Yao, Y. Hui, N. Zhou, *Nano-Micro Lett.* **2023**, *15*, 180.

[18]   A. Marino, J. Barsotti, G. De Vito, C. Filippeschi, B. Mazzolai, V. Piazza, M. Labardi, V. Mattoli, G. Ciofani, *ACS Appl. Mater. Interfaces* **2015**, *7*, 25574.

[19]   X. Wen, B. Zhang, W. Wang, F. Ye, S. Yue, H. Guo, G. Gao, Y. Zhao, Q. Fang, C. Nguyen, X. Zhang, J. Bao, J. T. Robinson, P. M. Ajayan, J. Lou, *Nat. Mater.* **2021**, *20*, 1506.

[20]   A. Desponds, A. Banyasz, D. Chateau, A. Tellal, A. Venier, S. Meille, G. Montagnac, J. Chevalier, C. Andraud, P. L. Baldeck, S. Parola, *Small* **2021**, *17*, 2102486.

[21]   F. Kotz, A. S. Quick, P. Risch, T. Martin, T. Hoose, M. Thiel, D. Helmer, B. E. Rapp, *Adv. Mater.* **2021**, *33*, 2006341.

[22]   H. Wang, W. Zhang, D. Ladika, H. Yu, D. Gailevičius, H. Wang, C. Pan, P. N. S. Nair, Y. Ke, T. Mori, J. Y. E. Chan, Q. Ruan, M. Farsari, M. Malinauskas, S. Juodkazis, M. Gu, J. K. W. Yang, *Adv. Funct. Mater.* **2023**, 2214211.

[23]   A. Vyatskikh, R. C. Ng, B. Edwards, R. M. Briggs, J. R. Greer, *Nano Lett.* **2020**, *20*, 3513.

[24]   J. Winczewski, M. Herrera, C. Cabriel, I. Izeddin, S. Gabel, B. Merle, A. Susarrey Arce, H. Gardeniers, *Adv. Opt. Mater.* **2022**, *10*, 2102758.

[25]   D. W. Yee, M. L. Lifson, B. W. Edwards, J. R. Greer, *Adv. Mater.* **2019**, *31*, 1901345.

[26]   H. Xia, Q.-D. Chen, H.-B. Sun, H.-T. Fan, L. Guo, T. Zhang, Y.-L. Zhang, *Opt. Lett. Vol. 35, Issue 10, pp. 1695-1697* **2010**, *35*, 1695.

[27]   J. Bauer, C. Crook, T. Baldacchini, *Science* **2023**, *380*, 960.

[28]   D. Gailevičius, V. Padolskytė, L. Mikoliūnaitė, S. Šakirzanovas, S. Juodkazis, M. Malinauskas, *Nanoscale Horizons* **2019**, *4*, 647.

[29]   A. Desponds, A. Banyasz, G. Montagnac, C. Andraud, P. Baldeck, S. Parola, *J. Sol-Gel Sci. Technol.* **2020**, *95*, 733.

[30]   L. Brigo, J. E. M. Schmidt, A. Gandin, N. Michieli, P. Colombo, G. Brusatin, *Adv. Sci.* **2018**, *5*, 1800937.

[31]   H. Dory, P. Miele, C. Salameh, *Int. J. Appl. Ceram. Technol.* **2023**, *20*, 141.

[32]   T. A. Pham, D. P. Kim, T. W. Lim, S. H. Park, D. Y. Yang, K. S. Lee, *Adv. Funct. Mater.* **2006**, *16*, 1235.

[33]   Q. Hanniet, E. Petit, S. Calas-Etienne, P. Etienne, K. Aissou, C. Gervais, P. Miele, B. Charlot, C. Salameh, *Mater. Des.* **2022**, *223*, 111234.

[34]   I. Cooperstein, S. R. K. C. Indukuri, A. Bouketov, U. Levy, S. Magdassi, *Adv. Mater.* **2020**, *32*, 1.

[35]   J. Winczewski, M. Herrera, H. Gardeniers, A. Susarrey-Arce, *Chem. Commun.* **2023**, *59*, 3095.

[36]   T. Yu, C. H. Chen, X. F. Chen, W. Zhu, R. G. Krishnan, *Ceram. Int.* **2004**, *30*, 1279.

[37]   A. Dwivedi, A. N. Cormack, *J. Solid State Chem.* **1989**, *79*, 218.

[38]   X. Meng, E. Li, W. Huang, Y. Bai, W. Ma, R. Wang, *Surf. Coatings Technol.* **2019**, *369*, 87.

[39]   P. Ptáček, E. Bartoníčková, J. Švec, T. Opravil, F. Šoukal, F. Frajkorová, *Ceram. Int.* **2015**, *41*, 115.

[40]   K. S. P. Karunadasa, C. H. Manoratne, H. M. T. G. A. Pitawala, R. M. G. Rajapakse, *J. Phys. Chem. Solids* **2019**, *134*, 21.

WILEY-VCH

[41] M. E. B. Andrew K. Galwey, Ed. , in *Therm. Decompos. Ion. Solids*, Elsevier Science, **1999**, pp. 345–364.

[42] J. P. Winczewski, S. Zeiler, S. Gabel, A. Susarrey-Arce, J. G. E. Gardeniers, B. Merle, *Mater. Des.* **2023**, *232*, 112142.

[43] R. S. André, S. M. Zanetti, J. A. Varela, E. Longo, *Ceram. Int.* **2014**, *40*, 16627.

[44] S. M. Hope, S. Kundu, C. Roy, S. S. Manna, A. Hansen, *Front. Phys.* **2015**, *3*, 1.

[45] M. Pelanconi, M. Barbato, S. Zavattoni, G. L. Vignoles, A. Ortona, *Mater. Des.* **2019**, *163*, 107539.

[46] C. Xie, D. Yan, H. Li, S. Du, W. Chen, Y. Wang, Y. Zou, R. Chen, S. Wang, *ACS Catal.* **2020**, *10*, 11082.

[47] S. Cao, F. F. Tao, Y. Tang, Y. Li, J. Yu, *Chem. Soc. Rev.* **2016**, *45*, 4747.

[48] B. Koo, K. Kim, J. K. Kim, H. Kwon, J. W. Han, W. C. Jung, *Joule* **2018**, *2*, 1476.

[49] G. Taglieri, M. Tersigni, P. L. Villa, C. Mondelli, *Int. J. Inorg. Mater.* **1999**, *1*, 103.

[50] P. Makuła, M. Pacia, W. Macyk, *J. Phys. Chem. Lett.* **2018**, *9*, 6814.

[51] L. S. Cavalcante, V. M. Longo, M. Zampieri, J. W. M. Espinosa, P. S. Pizani, J. R. Sambrano, J. A. Varela, E. Longo, M. L. Simões, C. A. Paskocimas, *J. Appl. Phys.* **2008**, *103*, 063527.

[52] A. B. Lavand, Y. S. Malghe, *J. Therm. Anal. Calorim.* **2014**, *118*, 1613.

[53] P. Stoch, J. Szczerba, J. Lis, D. Madej, Z. Pędzich, *J. Eur. Ceram. Soc.* **2012**, *32*, 665.

[54] Z. F. Hou, *Phys. B Condens. Matter* **2008**, *403*, 2624.

[55] K. Hkiri, H. E. A. Mohamed, B. S. Khanyile, C. Mtshali, M. Nkosi, M. Ben Salem, M. Maaza, M. Zouaoui, *Surfaces and Interfaces* **2021**, *25*, 101259.

[56] L. S. Cavalcante, A. Z. Simões, J. C. Sczancoski, V. M. Longo, R. Erlo, M. T. Escote, E. Longo, J. A.

WILEY-VCH

Varela, *Solid State Sci.* **2007**, *9*, 1020.

[57] A. M. Huerta-Flores, L. M. Torres-Martínez, D. Sánchez-Martínez, M. E. Zarazúa-Morín, *Fuel* **2015**, *158*, 66.

[58] I. I. Leonidov, V. I. Tsidilkovski, E. S. Tropin, M. I. Vlasov, L. P. Putilov, *Mater. Lett.* **2018**, *212*, 336.

[59] B. Henderson, *Contemp. Phys.* **2002**, *43*, 273.

[60] C. F. Klingshirn, *Semiconductor Optics*, Springer Berlin Heidelberg, Berlin, Heidelberg, **2012**.

[61] L. S. Cavalcante, J. C. Sczancoski, J. W. M. Espinosa, V. R. Mastelaro, A. Michalowicz, P. S. Pizani, F. S. De Vicente, M. S. Li, J. A. Varela, E. Longo, *J. Alloys Compd.* **2009**, *471*, 253.

[62] H. Abdou, S. K. Gupta, Y. Mao, *J. Lumin.* **2019**, *214*, 116599.

[63] L. R. Macario, M. L. Moreira, J. Andrés, E. Longo, *CrystEngComm* **2010**, *12*, 3612.

[64] E. C. Aguiar, A. Z. Simões, C. A. Paskocimas, M. Cilense, E. Longo, J. A. Varela, *J. Mater. Sci. Mater. Electron.* **2015**, *26*, 1993.

[65] V. H. Romero, E. De la Rosa, P. Salas, J. J. Velázquez-Salazar, *J. Solid State Chem.* **2012**, *196*, 243.

[66] M. Boffelli, W. Zhu, M. Back, G. Sponchia, T. Francese, P. Riello, A. Benedetti, G. Pezzotti, *J. Phys. Chem. A* **2014**, *118*, 9828.

[67] J.-M. Costantini, Y. Watanabe, K. Yasuda, M. Fasoli, *J. Appl. Phys.* **2017**, *121*, 153101.

[68] M. L. Moreira, J. Andrés, J. A. Varela, E. Longo, *Cryst. Growth Des.* **2009**, *9*, 833.

[69] K. Dhahri, M. Bejar, E. Dhahri, M. J. Soares, M. F. P. Graça, M. A. Sousa, M. A. Valente, *Chem. Phys. Lett.* **2014**, *610–611*, 341.

[70] Z. Wang, J. Zhang, G. Zheng, X. Peng, H. Dai, *J. Lumin.* **2013**, *144*, 30.

WILEY-VCH

[71]   C. Kayathiri, A. R. Balu, M. Suganya, G. Vinitha, Z. Delci, S. Balamurugan, M. Karthika, S. Anitha, A. Prabavathi, *Mater. Sci. Eng. B* **2022**, *278*, 115636.

[72]   N. Li, K. Tong, L. Yang, X. Du, *Mater. Today Energy* **2022**, *29*, 101100.

[73]   J. M. Aguirre-Cortés, A. I. Moral-Rodríguez, E. Bailón-García, A. Davó-Quiñonero, A. F. Pérez-Cadenas, F. Carrasco-Marín, *Appl. Mater. Today* **2023**, *32*, 101831.

[74]   J. J. Carey, K. P. McKenna, *J. Phys. Chem. C* **2019**, *123*, 22358.

[75]   D. N. Mueller, M. L. MacHala, H. Bluhm, W. C. Chueh, *Nat. Commun.* **2015**, *6*, 1.

[76]   S. K. Gupta, P. S. Ghosh, N. Pathak, R. Tewari, *RSC Adv.* **2015**, *5*, 56526.

[77]   X. Liu, J. Zhang, X. Ma, H. Sheng, P. Feng, L. Shi, R. Hu, Y. Wang, *J. Alloys Compd.* **2013**, *550*, 451.

[78]   V. M. Longo, L. S. Cavalcante, R. Erlo, V. R. Mastelaro, A. T. de Figueiredo, J. R. Sambrano, S. de Lázaro, A. Z. Freitas, L. Gomes, N. D. Vieira, J. A. Varela, E. Longo, *Acta Mater.* **2008**, *56*, 2191.

[79]   V. M. Longo, L. S. Cavalcante, M. G. S. Costa, M. L. Moreira, A. T. de Figueiredo, J. Andrés, J. A. Varela, E. Longo, *Theor. Chem. Acc.* **2009**, *124*, 385.

[80]   D. J. Lee, D. H. Kim, J. W. Park, Y. S. Lee, *J. Korean Phys. Soc.* **2011**, *59*, 2797.

[81]   D. Kan, T. Terashima, R. Kanda, A. Masuno, K. Tanaka, S. Chu, H. Kan, A. Ishizumi, Y. Kanemitsu, Y. Shimakawa, M. Takano, *Nat. Mater.* **2005**, *4*, 816.

[82]   D. Gailevičius, V. Padolskytė, L. Mikoliūnaitė, S. Šakirzanovas, S. Juodkazis, M. Malinauskas, *Nanoscale Horizons* **2019**, *4*, 647.

[83]   A. S. Patra, G. Gogoi, M. Qureshi, *ACS Omega* **2018**, *3*, 10980.

[84]   A. Rubano, D. Paparo, F. M. Granozio, U. Scotti di Uccio, L. Marrucci, *J. Appl. Phys.* **2009**, *106*, 103515.

Accepted Article

WILEY-VCH

Table of contents

J.P. Winczewski, J. Arriaga Dávila, M. Herrera-Zaldívar, F. Ruiz-Zepeda, R. Margoth Córdova-Castro, Camilo R. Pérez de la Vega, C. Cabriel, I. Izeddin, J.G.E. Gardeniers, and A. Susarrey-Arce

3D-architected alkaline-earth perovskites
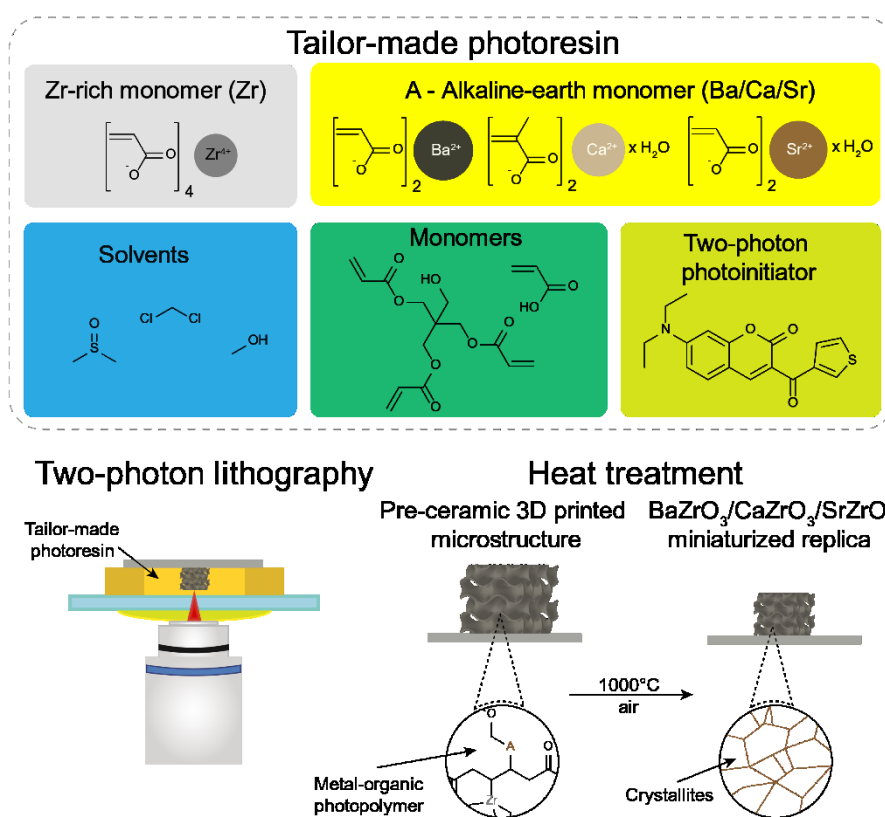
A newly developed approach enabling custom-made photoresists suited for additive manufacturing using two-photon lithography is introduced. The approach permits the production of 3D alkaline-earth

39

perovskite ($BaZrO_3$, $CaZrO_3$, and $SrZrO_3$) microarchitectures with sub-micrometer precision. The optical properties of such perovskite architectures are investigated using cathodoluminescence and wide-field photoluminescence emission to understand the defects and determine photoluminescence lifetimes.